Aust. J. Phys., 1995, **48**, 233–57

Basic and Applied Research at NTT and Postgraduate Education*

Tatsuya Kimura

Basic Research Laboratories, NTT, 3-1 Morinosato Wakamiya,
Atsugi-shi, Kanagawa 243-01 Japan.
Present address: Central Research Laboratories, NEC Corporation,
4-1-1 Miyazaki, Miyamae-ku, Kawasaki-shi, Kanagawa 216, Japan.

Abstract

Several current research topics, which are studied at NTT Basic Research Laboratories, are reviewed in the fields of semiconductor physics, quantum optics and biophysics. These topics include the surface structure transition of GaAs, InAs and Si, electron transport in low-dimensional structure, microcavity quantum-wire semiconductor lasers, quantum nondemolition measurement of fibre solitons, and artificial network development of cultivated neural cells.

1. Introduction

It would be appropriate to begin with a brief outline of our background, because the NTT Laboratories may be less well known outside of Japan. As a nationwide telecommunications company, and the leader in Japan, NTT puts much stress on R&D in telecommunication technologies. Since NTT was privatised in 1985, a considerable and slightly increasing percentage of financial and personnel resources has been invested in R&D.

In all the varied R&D activities of NTT, ranging from basic scientific research to developing practical telecommunication services, the NTT Basic Research Laboratories seek to carry out our mission of contributing to the academic community through advanced scientific research, and by providing innovative seeds for future telecommunication technologies. The Laboratories have nearly 200 researchers working in a broad range of fields such as human information science, computer science, quantum optics and optical materials, semiconductor physics, and materials science, as shown in Fig. 1.

One of the most important features of the Laboratories is our 'open-door' policy, which is intended to promote active exchange of scientific information and research personnel in the pre-competitive phase. We offer several programs to accommodate visiting foreign scientists, who might be permanent employees, invited scientists, postdoctoral fellows, or graduate trainees. Actually, these programs have already brought more than 100 scientists to our Laboratories during the last several years. The company supports each with an honorarium or monthly salary and also provides a corporate apartment at the employee rate.

* Refereed paper based on a plenary lecture given to the Sixth Asia Pacific Physics Conference and Eleventh Australian Institute of Physics Congress held at Griffith University, Brisbane, July 1994.

0004-9506/95/020233$10.00

◇Missions:

- Academic contribution through scientific research
- Innovative concepts for future technologies

◇Research areas:

- Human information science
- Computer science
- Quantum optics / optical materials
- Semiconductor physics
- Materials science

◇Research staff: ~200

including visiting scientists and post docs (about 10 %) and graduate course trainees

Fig. 1. Outline of the NTT Basic Research Laboratories.

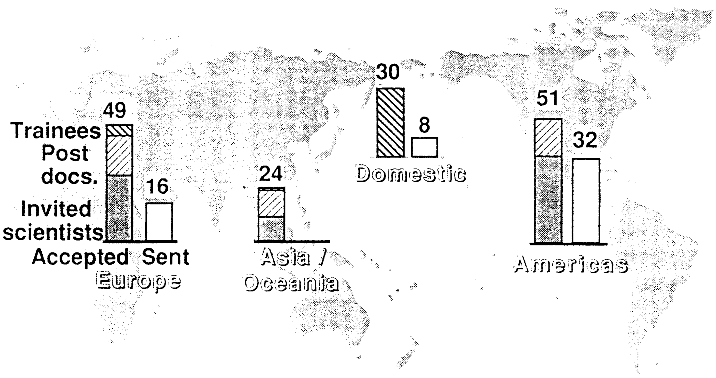

* As of end of 1993 FY

Fig. 2. Exchange of research scientists at NTT Basic Research Laboratories.

◇Open-door policy

- Exchange with non-profit research organizations
- Mutual personnel exchange and joint research

◇Freedom in research for excellent scientists

◇Advanced scientific research with advanced technological tools

◇Publication / participation in international journals and conferences

◇Evaluation and promotion

Fig. 3. Policy of the NTT Basic Research Laboratories.

Accommodation is an important consideration in and near Tokyo, where real estate is extremely expensive.

The system of postdoctoral fellowships is much the same as those in western countries, and is based on a contract for one or two years. During the last five years, we have hosted more than 50 postdoctoral fellows, who came from Europe, the United States, and Asia/Oceania, as shown in Fig. 2. They contributed to excellent achievements in joint research projects. In fact, most of the research results I am going to introduce in the latter part of this paper are the fruit of cooperative work by NTT's permanent staff and those visitors.

The Laboratories employ several other policies to facilitate their research activities. For example, research plans are usually made by adopting the opinions of scientists themselves, especially those who have made the most outstanding contributions. In a word, the Laboratories provide a university-level research environment to encourage and promote innovative scientific research. We offer research tools, publishing opportunities, and evaluation and promotion, as shown at the bottom of Fig. 3.

Among the various subjects we are studying at NTT Basic Research Laboratories, I would like to show you recent progress on several topics shown in Fig. 4, which I hope will excite your interest. I will review recent achievements in the areas of semiconductor physics, quantum optics, and neural science.

2. Surface Structure Transitions of GaAs, InAs and Si

Several years ago, one of our researchers invented an improved method of molecular beam epitaxy called migration-enhanced epitaxy, or MEE (Horikoshi *et al.* 1986). MEE features monoatomic control of growing layers, growth at low temperatures, growth of new and exotic materials, and growth of low-dislocation-density GaAs on a Si substrate, as shown in Fig. 5. In growing GaAs, Ga and As atoms are supplied separately and alternately. The step-flow growth is favoured by the enhanced atomic Ga migration on an As-stabilised growth surface.

The concept of MEE inspired basic studies in semiconductor physics, such as crystal growth mechanisms, semiconductor surfaces, nanometre-structure fabrication and mesoscopic electronics. Migration of adatoms on a semiconductor surface is a key mechanism in epitaxial growth. Enhanced adatom migration is crucial for high-quality epitaxy, because the migration over a wide area leads to a smooth grown surface. We calculated the migration potential of Ga adatoms on a reconstructed As-stabilised GaAs (001)–(2×4) surface by the *ab initio* pseudopotential method, as shown in Fig. 6. We found that the migration potential depends on the coverage of Ga adatoms. The dynamical behaviour of Ga on the GaAs surface during epitaxy was then simulated by the Monte Carlo method at finite temperature (Shiraishi *et al.* 1994).

The *ab initio* calculation showed that the long-bridge sites of the As dimer regions are most favourable energetically (by $0\cdot6$ eV) at low Ga coverage ($\theta \sim 0\cdot0625$), monolayer as shown in Fig. 7. In contrast, the missing dimer regions become more favourable (by $0\cdot3$ eV) as the Ga coverage increases ($\theta \sim 0\cdot1875$ monolayer). Based on the migration potential, the coverage dependence was confirmed by Monte Carlo simulation at the finite temperature of 600°C. The simulation showed that the Ga adatoms actually do occupy the As dimer region predominantly at the initial stage of epitaxial growth. As the number of Ga adatoms increases, the

◇Semiconductor physics

Surface structure transition of GaAs, InAs and Si

Electron transport in low-dimensional structure

◇Quantum optics

Microcavity quantum-wire semiconductor laser

Quantum nondemolition (QND) measurement of fiber soliton

◇Biological electronics

Artificial network development of cultivated neural cells

Fig. 4. Recent research topics of interest at NTT Basic Research Laboratories.

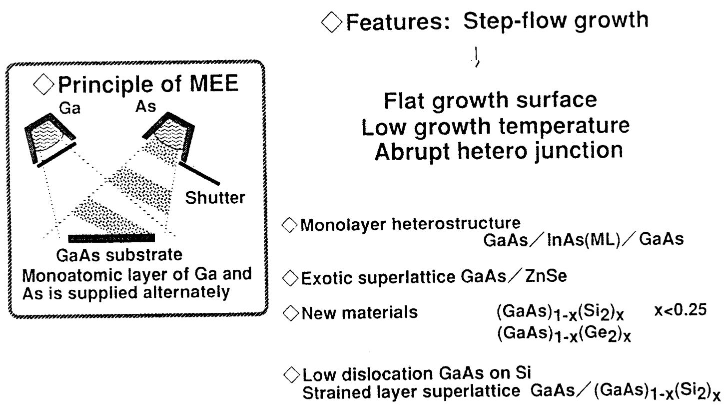

Fig. 5. Epitaxy of compound semiconductors—migration-enhanced epitaxy.

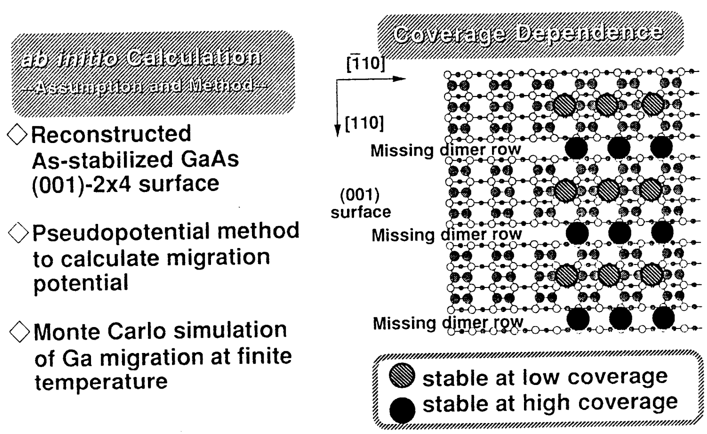

Fig. 6. Ga on a GaAs surface—calculation of migration potential.

missing dimer region is occupied by the Ga adatoms, in accordance with the coverage dependence of the migration potential. Both of these results show that the dynamic behaviour of Ga under the growth conditions is sensitive to the Ga coverage.

Next we discuss the surface structure transition on III–V semiconductor surfaces. Here, we focus on the difference between two arsenide crystals: GaAs and InAs. Their bulk stoichiometry is exactly 1 : 1, but the surface stoichiometry depends on the atmosphere to which the surface is exposed. Fig. 8 shows the reflected high-energy electron diffraction (RHEED) specular intensity as a function of temperature under As pressure. The top row here shows GaAs results and the bottom row shows data for InAs. Here, during the RHEED observation, we used a Faraday cup instead of a fluorescent screen. This allowed us to measure the diffraction intensity linearly over a wide dynamic range.

For each crystal, we grew a buffer layer at the temperature T_{growth}. The grown surface is stabilised by an As-monolayer and shows (2×4) structure. The temperature was gradually raised until a metastable (4×2) structure appeared, then the sample was slowly cooled. A striking difference was observed between the RHEED intensity of GaAs and that of InAs. For GaAs, it shows a gradual change from (4×2) to (2×4), always passing through an intermediate (3×1) structure. The GaAs surface structure changes smoothly, or continuously, between the metastable and As-stable structures. On the other hand, the RHEED intensity for InAs shows a discontinuity with a hysteresis gap of 10°C, which indicates a first-order transition (Yamaguchi and Horikoshi 1992, 1993*a*, 1993*b*).

A Monte Carlo simulation explains the difference in structure transition. The difference in the RHEED observation was reproduced with a certain lateral interaction between surface As atoms. If the lateral interaction is smaller than the critical value of $1{\cdot}76kT_{\text{tr}}$, the As atoms desorb individually, and the transition becomes continuous, as was observed in GaAs. In contrast, if the lateral interaction is larger than the critical value, the As atoms at the step edge desorb, and the domain of the metallic surface is broadened. The transition becomes discontinuous, as in the case of InAs RHEED observations. So, the difference can be explained by lateral interaction between surface As atoms (Yamaguchi and Horikoshi 1995*a*, 1995*b*).

To examine the origin of the different lateral interaction patterns, samples were observed by an atomic-resolution scanning tunneling microscope (STM) at elevated temperatures. The left-hand side of Fig. 9 shows the STM images of (2×4) structures for GaAs and InAs (001) surfaces. It is clearly observable that As-dimer rows and dimer-vacancy rows are formed in both GaAs and InAs, but there is a significant difference with respect to the uniformity of atomic structure. In GaAs, the dimer-vacancy row includes kinks, as shown in the GaAs STM image (arrowed) and illustrated schematically on the right-hand side in Fig. 9. The kink density increases when the sample is further annealed in a high vacuum. On the other hand, the dimer-vacancy row of InAs is quite straight, and it remains straight after further annealing. Thus the kinks in the dimer-vacancy row are more easily formed by thermal annealing in GaAs than in InAs. These kink observations can be related to the lateral interaction between surface As atoms. That is, strong lateral interaction results in uniform surface structure, as was observed in InAs.

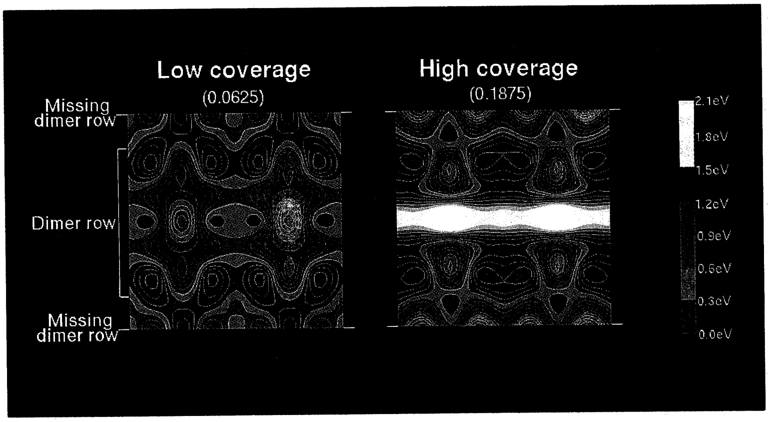

Fig. 7. Coverage dependence of the Ga migration potential.

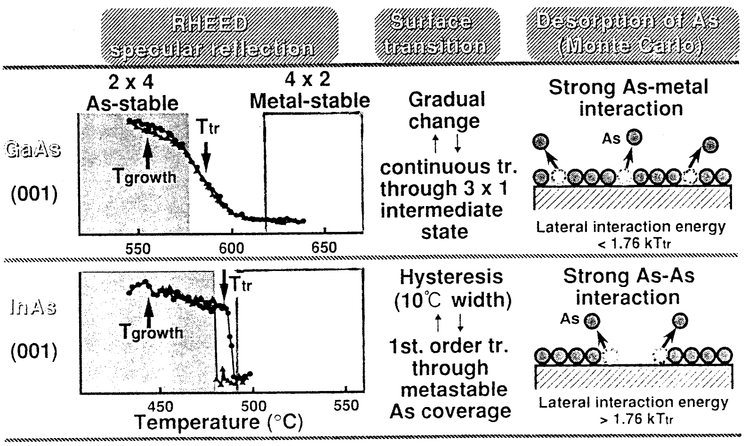

Fig. 8. Surface structure transition—GaAs versus InAs.

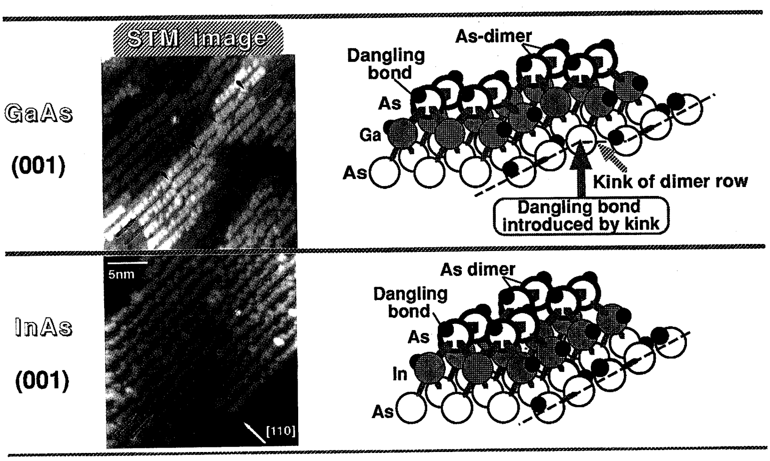

Fig. 9. STM image and surface structure—GaAs versus InAs.

Pashley and his coworkers pointed out that the kinks in the dimer-vacancy row are the origin of surface states (Pashley and Haberern 1991; Pashley *et al.* 1993). The difference in surface structure uniformity may cause the difference in electronic properties at the surface.

Fig. 10 shows the tunneling I–V characteristics of a GaAs (001) surface, which were measured by the tunneling current of the STM. The asymmetry observed in the I–V curve is explained by band-bending due to surface Fermi-level pinning. The number of kinks observed in the dimer-vacancy row is of the order of 10^{13} cm^{-2}, which is five times larger than is expected from the doping level (5×10^{17} cm^{-3}), and is high enough to cause Fermi-level pinning.

On the other hand, the tunneling I–V curve of InAs is quite symmetric, even at a low doping level (10^{16} cm^{-3}). The STM image of InAs, which shows a straight dimer-vacancy row, suggests a lower surface state density than in GaAs. The observed kink density is of the order of 10^{11} cm^{-2}, and remains constant even with intentional doping (3×10^{18} cm^{-3}). The symmetric I–V curve shows that the Fermi level is not pinned, at least in the midgap, in InAs, presumably because of the small kink density. This explains why the metal-deposited InAs surface shows no Schottky barrier height.

The surface electronic properties are closely related to the surface structure uniformity and surface phase transition, although these appear to be due to quite different physical phenomena. In order to understand the surface morphology, which is a crucial factor in epitaxial growth, we studied the behaviour of steps on a Si vicinal surface. The step configuration, including step densities and misorientation directions, can be controlled easily in the vicinal surface.

Fig. 11 shows a schematic diagram of step configurations on vicinal Si (111) surfaces at elevated temperatures, and the corresponding STM images. The vicinal (111) surface is uniformly covered with single-layer steps above the (1×1)–(7×7) phase-transition temperature T_c. The step arrangement below T_c, however, depends on the misorientation direction (Hibino *et al.* 1993; Hibino and Ogino 1994; Suzuki *et al.* 1993*a*, 1993*b*).

On a surface misoriented toward $[\bar{1}\bar{1}2]$, as shown on the left in Fig. 11, the transition temperature T_c is independent of the misorientation angle. The non-reconstructed surface with single-layer steps is transformed into the reconstructed surface with single- and triple-layer steps by the step-bunching process. The reconstruction starts at 830°C, step-bunching occurs at 828°C, and reconstruction is complete at 820°C.

The surface misoriented toward $[11\bar{2}]$ is also covered with single-layer steps at 740°C, although individual steps are not resolved in the STM image. As shown on the right-hand side of Fig. 11, the transition temperature T_c decreases with increasing misorientation angle, and the surface separates into (7×7)-reconstructed (111) facets and step bunches below the transition temperature T_c. At 739°C, stripe-shaped (111) facets appear. The transition temperature T_c for 10° misorientation toward $[11\bar{2}]$ is lower by 90°C than that misoriented toward $[\bar{1}\bar{1}2]$. As the temperature decreases further, the (111) surface area grows, and eventually groups of the bunched steps are transformed into (12×1)-reconstructed (331) facets.

From these observations, we know that the surface morphology depends on the temperature and the misorientation direction. The misorientation-direction

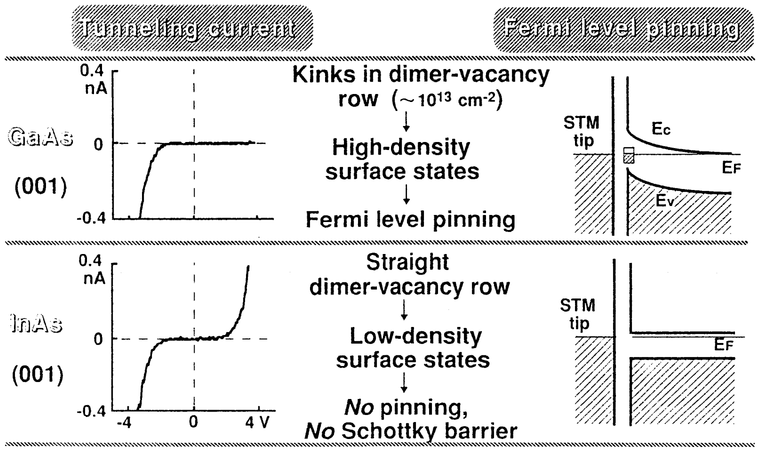

Fig. 10. Surface state and Fermi level pinning—GaAs versus InAs.

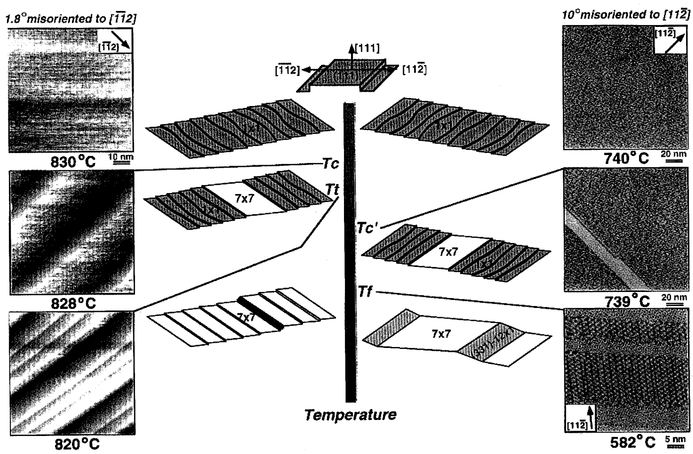

Fig. 11. Phase transition of the vicinal Si (111) surface.

	1st generation 1970's	2nd generation 1980's	3rd generation 1990's
Concept	· Superlattices · Quantum wells · 2DEG in MOS · Modulation doping · Bandgap engineering · Resonant tunneling	· Strained layer superlattices · Quantum confined Stark effect ---Wavefunction engineering	· Quantum-wires/-boxes · Quantum point contacts · Electron waveguides · Coulomb blockade
Tech-nology	· MBE · MOCVD	· EB lithography · X-ray lithography · Focused ion beam implantation · Monolayer growth ---MEE, ALE	· Growth on patterned substrates ---self-assembly · Integrated vacuum processing · STM processing
Device	· HEMT* · Quantum well laser*	· Heterobipolar transistor · Resonant tunneling tr. · QW IR detector · Surface emitting laser · Superlattice APD · Electro-optical device	· Electron WG devices · Electron-wave interference devices · Single-electron devices · Quantum-wire/-box lasers

* Commercialized

Fig. 12. Three generations of quantum functional devices.

dependence can be explained by the free energy difference of individual steps. Understanding the surface morphology in vicinal surfaces is important in controlling epitaxy, because vicinal substrates are used in growing GaAs on Si substrates.

3. Electron Transport in Low-dimensional Structures

Since the 1970s, there has been remarkable progress in physics research and in applications of semiconductor quantum effect device research, as shown in Fig. 12. The first generation of quantum wells and modulation doping led to quantum-well lasers and high-electron-mobility transistors using materials made with MBE and MOCVD technology. These concepts were perfected in the 1980s, and the new concepts of strained superlattices and the quantum confined Stark effect emerged.

Second-generation development of nanostructure lithography and monolayer growth technologies brought about a variety of novel devices such as resonant tunneling transistors and electro-optic devices. For the third generation, practical applications of one- and zero-dimensional structures, or quantum wires and boxes, have become the new research topics of the 1990s, and novel technologies such as growth on patterned substrates and STM processing have been developed for high-precision control of device dimensions. We expect that exciting research on these low-dimensional structures will open the way for new concepts of future devices, which may include single-electron devices, quantum-wire and quantum-box lasers, and so on.

Electron transport in semiconductor nanostructures has been studied mainly in systems based on GaAs materials. This is because GaAs has a long electron mean free path at low temperatures, and is suitable for ballistic device studies. Turning from GaAs, we have recently focused on systems based on InGaAs materials. Fig. 13 shows a comparison of the parameters of InGaAs- and GaAs-based modulation-doped heterostructures. At the low temperature of $1 \cdot 5$ K, the GaAs system has a high mobility, exceeding $10^6\ \mathrm{cm^2\,V^{-1}\,s^{-1}}$, which enables excellent ballistic device performance. However, the performance readily degrades at high temperatures due to the strong reduction in mean free path. The InGaAs system, on the other hand, retains a relatively high electron mobility even at room temperature. Furthermore, it has a high electron density, which is nearly one order of magnitude higher than that of GaAs. Consequently, the InGaAs system's electron mean free path at room temperature is five times that of the GaAs system. The high electron density is also favourable for reducing lateral depletion during microfabrication, and for achieving strong lateral confinement (Hirayama and Tarucha 1993).

In addition, the effective electron mass in an InGaAs lattice matched to InP is 67% that of GaAs, so we expect a large state separation in quantum wires and boxes formed in the InGaAs system. These features make the InGaAs system attractive for achieving a large quantum effect and high-temperature operation of ballistic devices. In this section, we demonstrate the characteristics of ballistic transport in two-, one- and zero-dimensional systems.

Fig. 14 shows two-dimensional ballistic transport in an InGaAs modulation-doped structure. We scanned a Ga-focused ion beam on the surface of the modulation-doped structure to write a small square pattern with four terminals, one at each corner. The implanted region becomes insulating, and the accompanying depletion region imposes lateral confinement on the 2D electrons. The geometrical

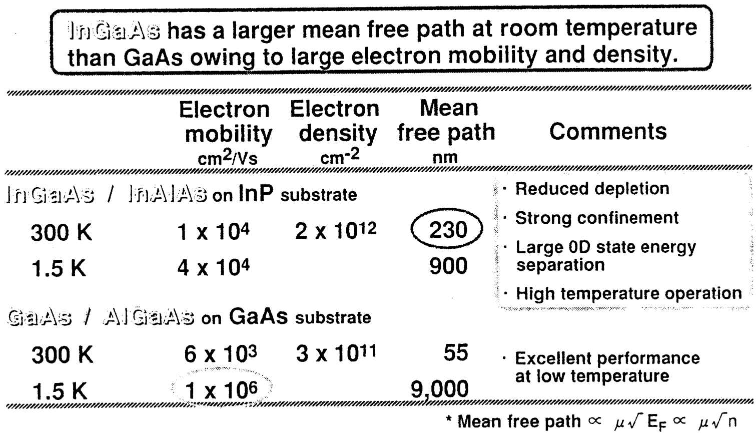

InGaAs has a larger mean free path at room temperature than GaAs owing to large electron mobility and density.

	Electron mobility cm^2/Vs	Electron density cm^{-2}	Mean free path nm	Comments
InGaAs / InAlAs on InP substrate				· Reduced depletion · Strong confinement · Large 0D state energy separation · High temperature operation
300 K	1 x 10^4	2 x 10^{12}	230	
1.5 K	4 x 10^4		900	
GaAs / AlGaAs on GaAs substrate				· Excellent performance at low temperature
300 K	6 x 10^3	3 x 10^{11}	55	
1.5 K	1 x 10^6		9,000	

* Mean free path $\propto \mu\sqrt{E_F} \propto \mu\sqrt{n}$

Fig. 13. Ballistic transport in InGaAs—comparison with GaAs.

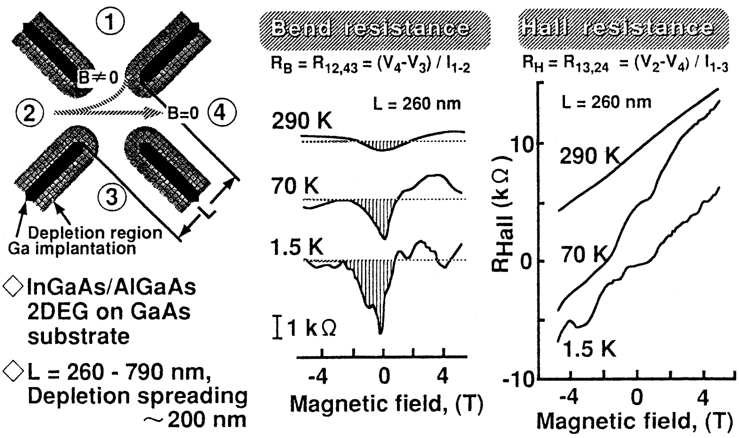

Fig. 14. Two-dimensional ballistic transport in an InGaAs modulation-doped structure.

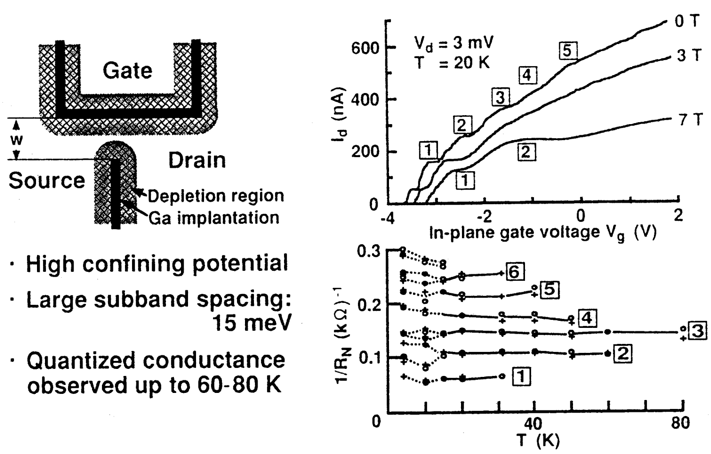

Fig. 15. One-dimensional ballistic transport in an InGaAs in-plane gated point contact.

device size defined by the implantation was reduced to 260 nm, which includes a total depletion spreading of 200 nm. This is significant because its minimum size is nearly half that formed in GaAs modulation-doped structures.

It is well known that the bend resistance and Hall resistance characteristics of a small four-terminal device give evidence of ballistic transport. Bend resistance is defined by the voltage difference between terminals 4 and 3 divided by the injected current from terminal 1 to 2. The resistance becomes negative when electrons injected at a current terminal 2 travel ballistically across the square region and enter voltage terminal 4. Application of a magnetic field disturbs the ballistic path and the negative resistance smears out. The curves at the centre show the bend resistance versus magnetic field characteristics of the 260 nm device in the temperature range from 1·5 to 290 K. We observe a negative resistance dip at zero field up to 290 K, which indicates the existence of 2D electrons traveling ballistically across the square region even at room temperature.

On the other hand, Hall resistance is defined by the voltage difference between terminals 2 and 4 divided by the injected current from terminal 1 to 3. This is shown on the right in Fig. 14 as a function of magnetic field. The Hall resistance shows quenching around zero magnetic field at 1·5 and 70 K. This quenching appears if electrons injected at current terminal 2, which travel ballistically in the square region, do not enter voltage terminal 1. A weak nonlinearity in the Hall resistance curve at 290 K also arises from the ballistic nature of electrons.

Fig. 15 shows 1D ballistic transport in an InGaAs in-plane-gated point contact. The device was also defined by Ga-focused ion beam implantation. The region surrounding the implanted line works as a planar gate, so that voltage applied to the gate controls the depletion width. 1D sub-bands are formed in the most constricted region between the source and drain, which leads to quantised conductance (Bever *et al.* 1995).

The top right figure shows the source–drain current versus gate voltage measured at 20 K for various magnetic fields. In the absence of a magnetic field, we observe five quantised conductance steps. Application of a magnetic field widens the 1D sub-band spacing, and extends the quantised conductance plateau. From this magnetic field dependence, we estimate a large 1D sub-band spacing of 15 meV. This value is at least three times larger than that in conventional GaAs point contacts, indicating the high confining potential that can be achieved in the InGaAs system. As the temperature increases, the quantisation steps are smeared out. Nevertheless, we can distinguish quantised conductance up to 80 K, as shown in the bottom right figure.

Fig. 16 shows the single-electron charging effect observed in transport through a zero-dimensional region. We used the same ion implantation technique to form a small dot between the source and drain. In this device, in-plane gates G_L and G_R control the tunneling barrier heights between the dot and source and between the dot and drain. The gate G_C controls the number of electrons in the dot (Fujisawa *et al.* 1994).

Addition of one electron in the central dot raises the electrostatic potential. When the overall capacitance of the dot is small enough, so that the change in electrostatic potential or charging energy is much larger than the thermal energy, the second electron coming in is blocked by the first electron. The source–drain conductance then becomes a maximum when the Fermi energy of the source and

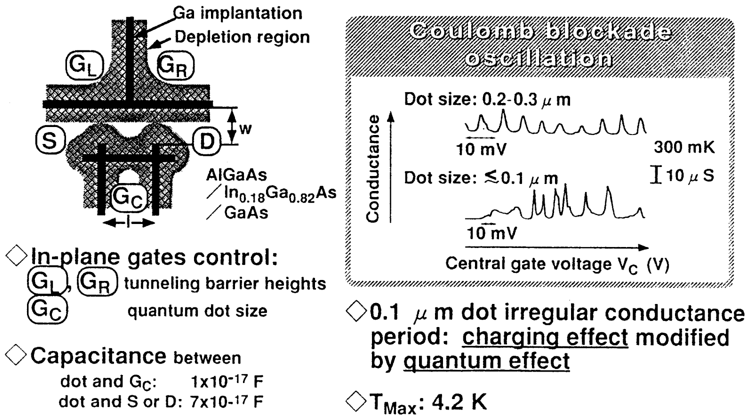

Fig. 16. Single-electron charging effect—transport through the zero-dimensional region.

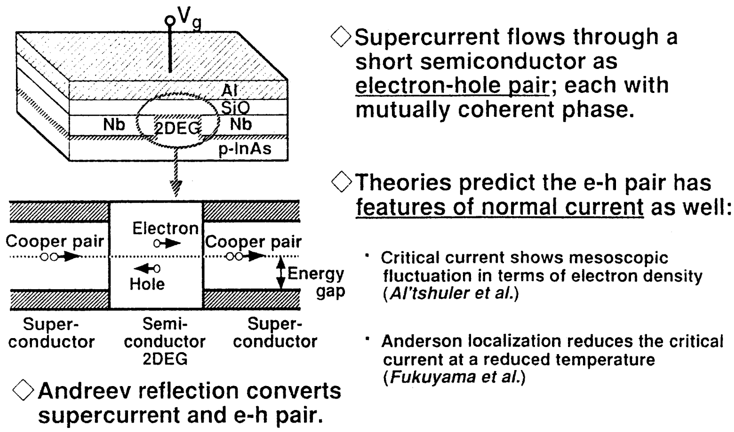

Fig. 17. Mesoscopic effects in an S/N/S junction—schematic of a fabricated junction.

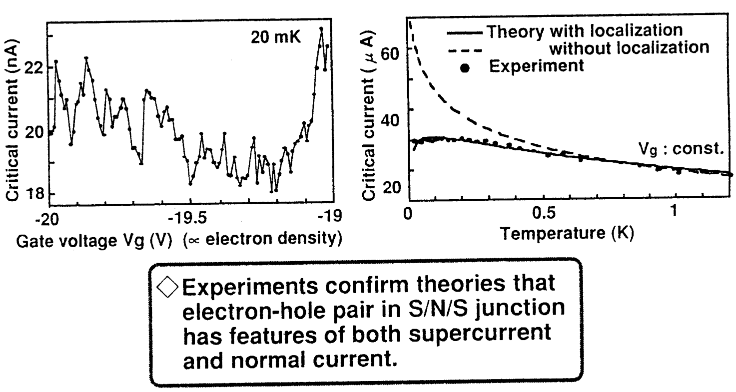

Fig. 18. Mesoscopic effects in an S/N/S junction—the critical current.

drain is higher than the chemical potential of the dot by an amount equal to the charging energy, or is otherwise zero. The change in the dot's chemical potential is a function of central gate voltage. Therefore, the conductance oscillates as a function of the central gate voltage, with the voltage period given by the single charge divided by the gate capacitance.

The upper curve in the right figure shows the periodic Coulomb oscillation observed in a device with a dot diameter of $0 \cdot 2$ to $0 \cdot 3$ μm. However, when the dot is smaller than $0 \cdot 1$ μm, the conductance oscillation becomes aperiodic. In such a small dot, the quantum-mechanical effect makes the 0D sub-band spacing large and comparable to the charging energy. Then the conductance oscillation period is restricted by the sum of sub-band spacing and charging energy. The 0D states are not evenly spaced, due to degeneracy and non-circular lateral confinement. So the irregular conductance period for the $0 \cdot 1$ μm dot comes from the charging effect modified by the quantum effect in the highly confined dot. The evaluated charging energy in these devices was about 2 meV, which gives a maximum temperature of $4 \cdot 2$ K for the observation of conductance oscillation.

We expect that the highest operating temperature, approaching 77 K, can be achieved in an InGaAs single-electron transistor. To raise the operating temperature further, it is probably necessary to develop new device configurations, such as using a dot a few tens of nm in diameter coupled to reservoirs through high, narrow heterojunction barriers.

A semiconductor or a normal metal of mesoscopic size will show current fluctuation due to electron interference effects. This phenomenon is called universal conductance fluctuation (UCF). Such fluctuations cannot occur in a bulk superconductor, because their quantum state is decided by the phase of the Cooper pairs. However, in a mesoscopic superconductor/normal metal/superconductor (S/N/S) junction, it is already known that the supercurrent flows through the junction as an electron–hole pair. To see just how the electron interference affects the superconducting current flowing across the S/N/S junction, we probed the issue experimentally (Takayanagi *et al.* 1995*a*, 1995*b*).

The top left of Fig. 17 is a schematic cross-sectional view of a fabricated junction. The supercurrent flows across the two-dimensional electron gas formed in the inversion layer of the p-type InAs substrate. Incident electrons from the semiconductor side to the junction are transformed into Cooper pairs in the superconductor, and for each, a hole is reflected back in the semiconductor by the Andreef reflection process. The supercurrent is carried by an electron–hole pair in the semiconductor. The pair creates a supercurrent because it is mutually coherent in phase.

We should note that there are two theories which predict that the electron–hole pair has features of a normal current as well. Al'tshuler *et al.* (1987) showed that the critical current (maximum supercurrent) of the S/N/S junction shows mesoscopic fluctuations as a function of the electron density of the normal metal due to an interference effect. Also, Fukuyama and Maekaw (1986) predicted that the critical current would decrease with decreasing temperature due to the Anderson localisation effect. These two predictions have been verified experimentally for the Nb/InAs/Nb junction.

The left of Fig. 18 shows that the critical current fluctuates as a function of the gate voltage. In this case, the temperature is 20 mK. The critical current fluctuation is analogous to the conductance fluctuation of the two-dimensional electron gas (2DEG) measured at the same time. The gate voltage induces a change in the 2DEG density, and the electron density variation causes a change in Fermi wavelength. From this, we infer that the critical current fluctuation is due to electron interference. The magnitude of the fluctuation is about 2 nA, and the typical period in terms of the gate voltage is about 100 mV. These magnitudes agree with theoretical calculation.

Next, I would like to show how the Anderson effect influences the critical current. The figure on the right shows the measured critical current as a function of temperature at zero gate voltage. The saturated critical current at low temperatures is explained by Anderson localisation caused by Coulomb interaction between electrons. The experimental results agree quite well with the theory, depicted by the solid line, which takes account of the localisation effect. This shows that the Coulomb interaction plays an important role in superconducting transport at the S/N/S junction at low temperatures.

The two experiments confirm theories that the electron–hole pair in the S/N/S junction has the features of both supercurrent and normal current.

4. Microcavity Quantum-wire Semiconductor Laser

Advanced crystal growth and processing technologies make it possible to fabricate semiconductor mesoscopic structures on a nanometre scale. Since the technology based on quantum-well structure is now established for producing semiconductor lasers, the fabrication and optical characterisation of quantum-wire and quantum-dot structures are now of great interest in terms of possible device applications. The enhanced density of states in these structures shown in Fig. 19 is expected to improve optical gain and optical nonlinearity.

The difficulty in developing a practical quantum-wire laser resides in how to fabricate a uniform, high-density array of quantum wires which are free from contamination and defects. Fig. 20 illustrates a method of fabricating high-density quantum wires directly by metal–organic chemical vapour deposition (MOCVD). A (001) GaAs vicinal substrate, misoriented toward the $[\bar{1}10]$ direction, is used in this growth. The regular staircase of GaAs monolayer terraces is produced by an appropriate pre-growth procedure. Precisely controlled half-monolayers of GaAs and AlAs are alternated. The growth cycle is repeated so as to produce a vertical stack of narrow stripes of GaAs and AlAs, which are arranged side by side. A lateral superlattice with compositional periodicity parallel to the grown surface is called a fractional-layer superlattice (FLS) (Fukui *et al.* 1988; Saito *et al.* 1993*a*).

The photograph on the right is a transmission electron microscope (TEM) image of the surface. You can see the uniform and densely arranged quantum wires formed over a wide area, $0\cdot4\times0\cdot5\ \mu m^2$. The superlattice period is 8 nm, which corresponds to a substrate tilt angle of 2°. The advantage of having quantum wires fabricated directly by crystal growth is that they are free from processing damage and impurities.

The microcavity effect is briefly reviewed in Fig. 21. The microcavity here consists of a pair of distributed Bragg reflectors, and a central spacer layer which includes an optical gain medium. It is known that spontaneous emission from an optical gain medium is not an immutable property of the gain medium, but can

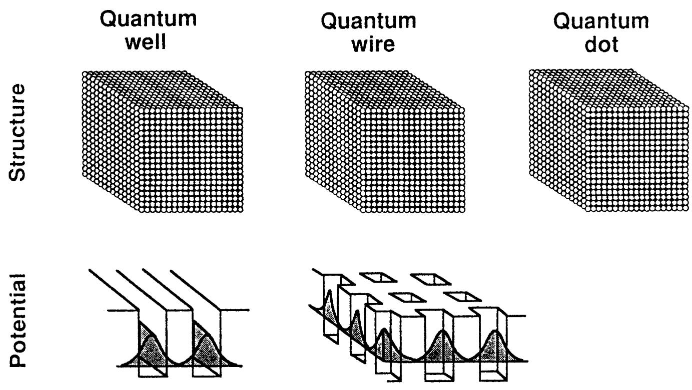

Fig. 19. Enhanced density of states in mesoscopic structures.

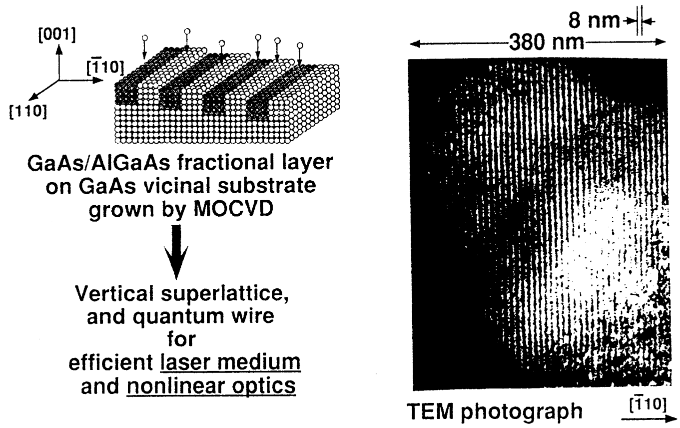

Fig. 20. Fractional-layer superlattice grown by MOCVD.

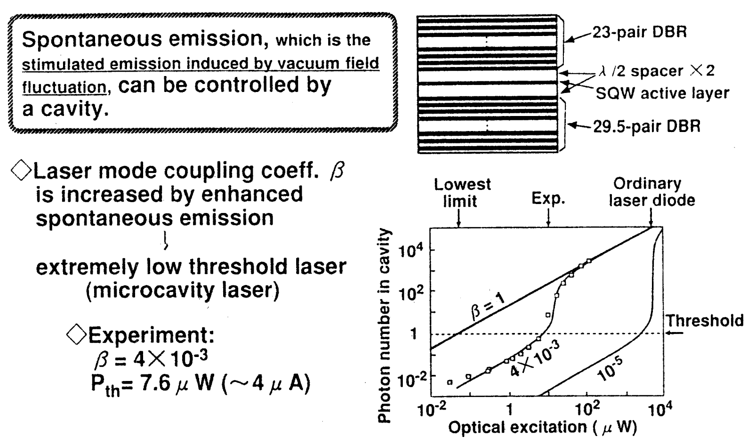

Fig. 21. Spontaneous emission controlled by a cavity.

be controlled by cavity resonance conditions. This can be explained by modified vacuum field fluctuation which induces spontaneous emission (Horowitz *et al.* 1992; Machinaga *et al.* 1993).

When the thickness of the central spacer layer is adjusted to one wavelength, the optical field is confined at the centre of the spacer layer, where the gain medium exists. The optical field is strongly coupled to the optical dipole in the gain medium. Thus the spontaneous emission is efficiently channelled into the single-cavity resonance mode, and the β value markedly improves in the microcavity laser. The enhancement in β in the microcavity lowers the lasing threshold by more than two orders of magnitude, compared with those in ordinary waveguide lasers. For β approaching 1, even 'thresholdless' lasing can be expected.

The FLS is applied to a semiconductor laser with a vertical microcavity. The quantum-wire thickness is 8 nm, the width is 6 nm, and the period is 8 nm. The FLS wire array is cladded by a short-period superlattice 20 nm thick. The superlattice acts as a barrier for carrier confinement in the vertical direction, as shown in Fig. 22.

The stack of quantum-wire arrays is sandwiched between highly reflective dielectric coating mirrors. Laser oscillation in the quantum-wire microcavity was demonstrated by optical pumping at room temperature. The threshold fluence was 7 pJ μm^{-2}. The output was found to be linearly polarised parallel to the quantum wire as the result of carrier confinement in the wire. The coupling coefficient of spontaneous photons into lasing mode, β, is around 5×10^{-4}, which is 100 times larger than in conventional semiconductor lasers.

The quantum-wire microcavity is an advanced concept in laser design, which combines the advantages of both carrier confinement in the quantum wire and optical confinement in the microcavity. The efficiency of electron-to-photon conversion improves considerably due to the sharply peaked density of states in the quantum wire. A large fraction of the photons emitted are coupled into the laser mode in the microcavity. The quantum-wire microcavity laser combines these advantageous features, and this combination will lead to lasers with extremely low thresholds and minimal size (Chavez-Pirson *et al.* 1993, 1994).

The FLS structure was also applied to a current-injection quantum-wire laser (Saito *et al.* 1993*b*). Fig. 23 shows a schematic view of the FLS quantum-wire laser with a stripe electrode. The FLS active layer is almost the same as in the previous microcavity laser, except that the superlattice barrier layers are impurity-doped for current injection.

Two kinds of laser device with different electrode stripe geometries, that is, parallel and perpendicular to the wire direction, were fabricated. Laser oscillation was observed with pulsed current injection below 200 K for both electrode configurations. An anisotropic gain, which is another important feature of the quantum-wire, manifested itself in the threshold current and oscillation wavelength, which clearly depend on the stripe directions. When the stripe is perpendicular to the quantum wire and the electric field is parallel to the wire, the threshold is lower and the oscillation occurs at a longer wavelength. This is attributable to the anisotropic gain induced by the quantum confinement in the FLS quantum wire. The heavy-hole-related optical dipole couples more efficiently with the photon when the electric field is parallel to the quantum wire. If vertical cavity configuration is employed, this in-plane anisotropy is expected to

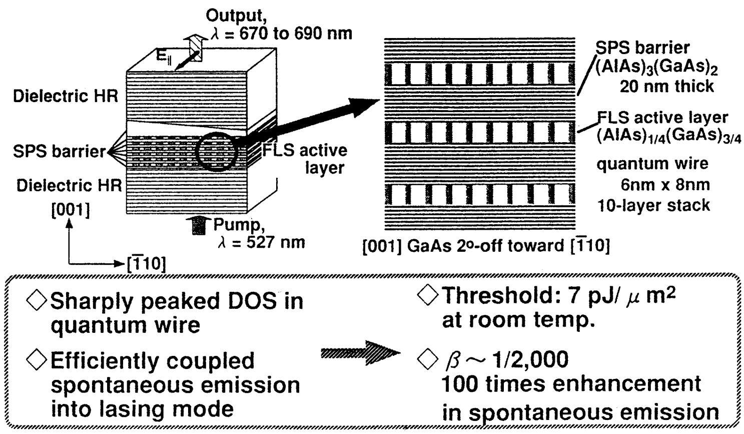

Fig. 22. Quantum-wire microcavity laser—using a fractional-layer superlattice.

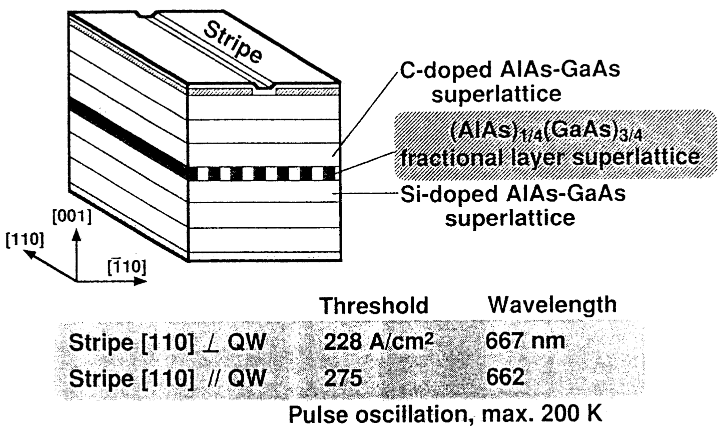

Fig. 23. Quantum-wire laser—using a fractional-layer superlattice.

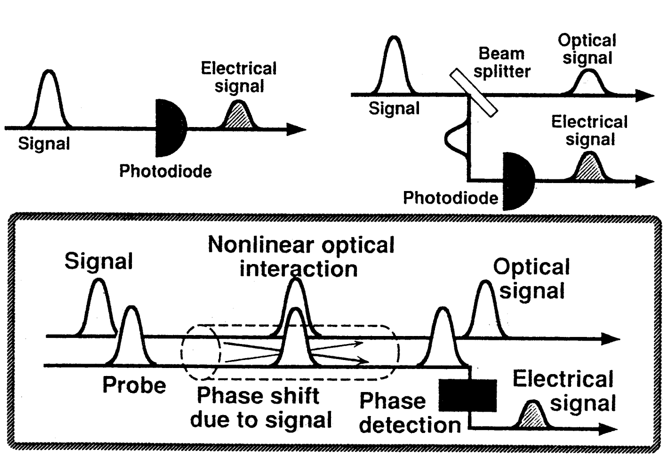

Fig. 24. Two techniques for quantum nondemolition measurements.

lead to a new class of optical switches which can assign information to the lasing polarisation states.

To take full advantage of the attractive features of such quantum-wire lasers for practical device applications, further improvement in FLS quality and microcavity performance is necessary.

5. Quantum Nondemolition Measurement of Fibre Solitons

Fig. 24 compares conventional optical signal measurement techniques with back action evasion (BAE) measurement that allows one to demonstrate quantum nondemolition (QND) measurement of the photon number of optical solitons (Drummond *et al.* 1993). Optical signal measurement using a photodiode produces an electrical signal, while simultaneously demolishing the original signal. Even with a beam splitter, a part of the signal is absorbed, and the optical signal is attenuated.

It is possible to perform a BAE measurement, as shown in the lower part of Fig. 24, which completely preserves the optical signal and adds no noise. Quantum solitons, that is, optical pulses with well defined quantum-mechanical properties, can easily be used in a measurement by having them collide in a low-loss single-mode optical fibre. A signal and a probe soliton of different velocities interact through a Kerr nonlinearity in the fibre. Since the interaction causes a phase shift of the probe in proportion to the signal photon number, the measured phase shift gives the signal photon number. After being measured, the signal soliton propagates freely, with its photon number unchanged. Heisenberg's uncertainty principle is not violated here, because the measurement increases uncertainty in the signal soliton's phase.

BAE measurement allows the determination of a quantum-mechanical observable without adding noise. This provides complete information about the signal soliton's photon number by measuring only the probe, leaving the signal unaltered as shown in Fig. 25. At the same time, BAE measurement reduces the quantum state of the measured observable.

Two successive BAE measurements that yield identical read-outs and do not change the quantum mechanical state of the signal constitute a quantum nondemolition measurement. Our main goal is to experimentally demonstrate the QND measurement by observing the quantum correlation between two successive BAE measurements.

Fig. 26 illustrates the experimental setup for BAE and QND measurement. A signal soliton is introduced into a polarisation-maintaining fibre $1\cdot5$ km long, along with identical probe and reference solitons, which move faster than the signal soliton. In the BAE experiment, the signal soliton is introduced midway between the probe and reference solitons, and it collides only with the probe, providing a phase shift measured in the interferometer with respect to the reference. The quantum correlation between the probe's phase and the signal's shot noise are determined to yield the BAE measurement.

The QND measurement is performed by adjusting the timing so that the signal soliton enters before the reference soliton and collides with both reference and probe solitons, as shown in Fig. 26 (Friberg *et al.* 1994). To observe the quantum correlation between two successive BAE measurements directly, we measured the phase noise difference between the probe and reference solitons at the output of the interferometer.

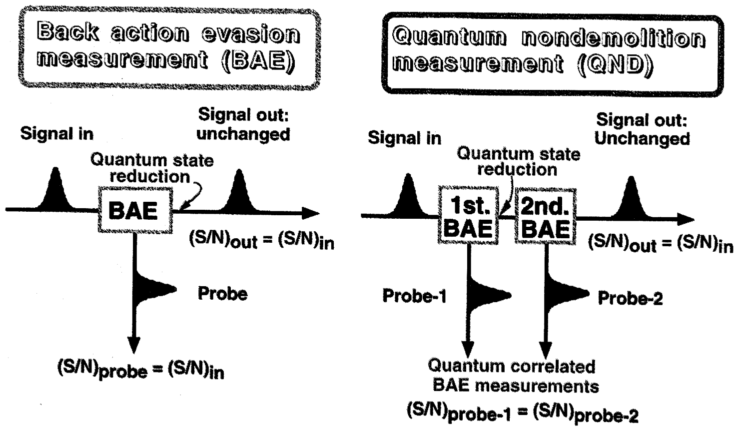

Fig. 25. Quantum nondemolition measurement—noise-free quantum-state-reduction measurement.

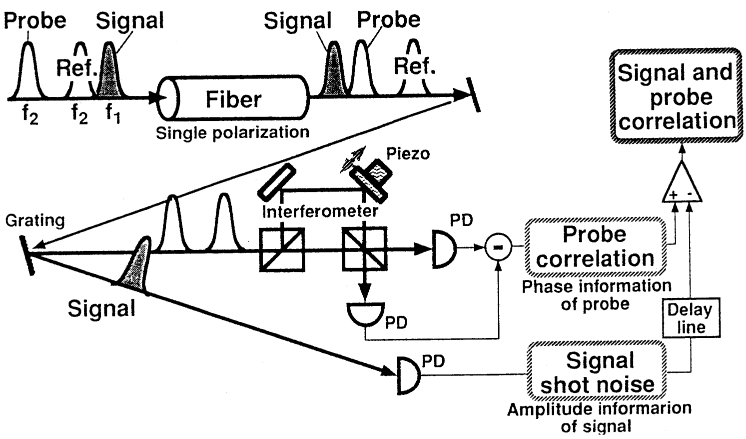

Fig. 26. Quantum nondemolition measurement—experimental setup.

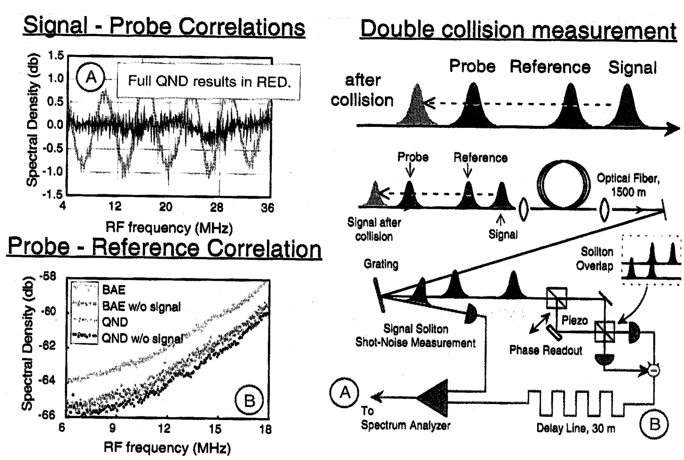

Fig. 27. Back action evasion measurement.

Fig. 27 illustrates the results on measurement. If the signal and the probe are correlated due to the Kerr effect, we observe a frequency modulation in the correlation trace because of an inserted delay line. This is shown in the top-left figure. In conjunction with a measured quantum-limited signal shot noise, this demonstrates successful BAE measurement of the signal photon number. The bottom-left figure shows that the probe–reference correlation increases by $1 \cdot 5$ dB, because of the shot-noise phase contribution in the correlation. This is to be compared with the double-collision experiment in Fig. 28.

The QND measurement is demonstrated in Fig. 28, which consists of two successive BAE measurements. The unmodulated red trace at the top left for the signal, probe and reference correlation suggests that the two BAE measurements give identical readouts. In the double-collision experiment, the phase noise difference is $0 \cdot 4$ dB, which is lower by more than 1 dB than that in the previous single-collision case. This shows that quantum correlation exists between the probe and the reference solitons, because both the probe and the reference solitons have nearly identical phase fluctuations due to the shot noise of the signal soliton.

This experiment is the first successful QND measurement of the signal photon number, or a quantum state in general, by direct observation of the quantum correlation between two successive measurements.

6. Artificial Network Development of Cultivated Neural Cells

The remarkable information-processing capacity of the human brain remains poorly understood, because of the huge number of neurons and the overwhelming complexity of mutual interconnections. Recent progress in cell culture technology has made it possible to routinely culture neurons to form synaptic connections among them. Culture systems of vertebrate neurons provide a useful means of studying the physiology of neurons and their networks.

In order to study the network functions, we need a technique for controlling the neural connections and for measuring the electrical activity of many neurons simultaneously. Even if the numbers of associated neurons in a cultured network are small, the resulting network of connections is usually complex enough for us not to recognise individual connections between particular neurons.

We fabricated silica glass substrates for growing simplified neural networks as shown in Fig. 29. The substrate consists of wells 150 μm square and connecting channels 20 μm wide, and 10 μm deep. A metal mask, with square openings at the positions corresponding to the wells, was put on the substrate in order to plate neurons only into the wells. A suspension of dissociated rat brain neurons was plated over the mask. After 12 hours, the metal was removed, then only the neurons adhering in the wells remained. The number of neurons in each well was controlled by varying the suspension density, and was typically about 20. Neurons within the same well formed synaptic connections in 2 or 3 days of starting the culture. Neurites then grew along the channel, inter-well synaptic connections were formed, and a simplified neural network was established (Jimbo *et al.* 1993).

We developed a substrate containing embedded electrodes, which enable multi-site recording of the neurons' electrical activity. Thus we can monitor the electrical activity of many neurons simultaneously and non-invasively.

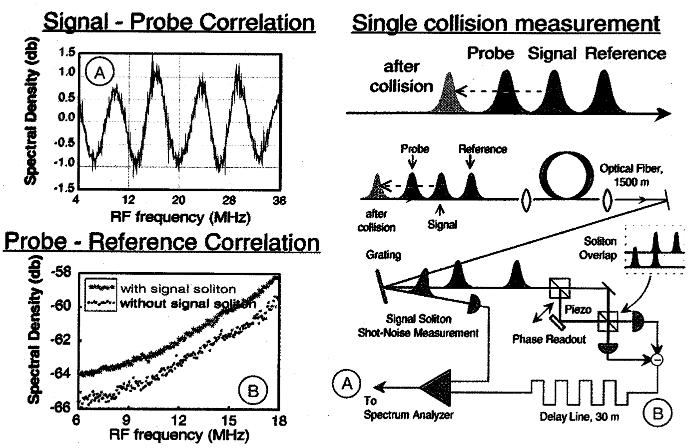

Fig. 28. Quantum nondemolition measurement with the double-collision experiment.

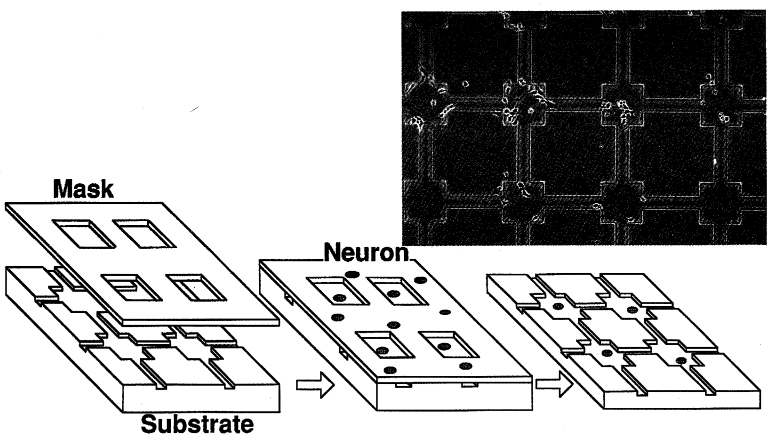

Fig. 29. A procedure for plating neurons in wells.

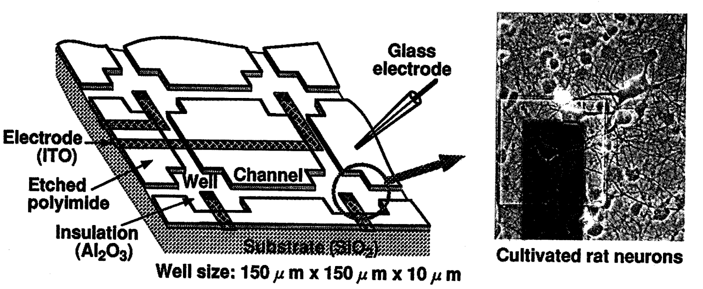

· **Simplified neural network for observing signal transmission and processing functions in identical neurons**

Fig. 30. Controlled neural cell growth on a patterned substrate with electrode.

The substrate was produced using microfabrication techniques. Indium tin oxide (ITO) is used for the electrodes, and aluminum oxide is used for an insulation film as shown in Fig. 30. In order to reduce the surface impedance of the ITO electrodes, platinum black was electro-deposited at the electrode tip. Wells and channels were formed by etching polyimide film, and embedded electrodes are used to excite and monitor electrical activity. When we measure the response of a specific neuron, a glass micropipette is also used.

The cultured neural networks provide a powerful research tool for stimulating and monitoring neurons' electrical activity stably over a long period. I will now discuss some recent results of our studies on the neural networks.

We cultured rat brain neurons on the substrate and monitored their electrical activity for about 4 weeks (Jimbo *et al.* 1994), as shown in Fig. 31. On the third day after the culture started, electrical signals are observed at several electrodes, but they show no correlation. Next day, periodic bursts appear at more than 30 s. intervals. The delay among bursts is large, but it becomes shorter as the days pass. The burst period became temporarily longer on the fifth and sixth days, but it became shorter after six days. Eventually, after 26 days, the electrical activity tended to an inherent profile, which consists of spikes and bursts. These changes in electrical activity correspond well to the timescale of neural network development. The absence of correlation on the third day suggests that there are no synaptic connections formed among neurons yet. They then start to form synaptic connections, which leads to periodic bursts. A long burst period and delay are symptomatic of the immaturity of the developing connections. We speculated that the burst period becomes longer around the fifth and sixth days because inhibitory synaptic connections appear. The periodic burst is accompanied by a transient increase in calcium ion concentration, which is believed to play an important role in network development. During this period, the number of excitatory and inhibitory synaptic connections increase, and eventually the network changes into its mature form. To my knowledge, this is the first observation of electrical activity associated with neural network development. The periodic burst seems to play an important role in revealing the development process.

The neural network on the substrate is also useful for studying plasticity, because the network lives a very long time, as long as it receives electrical stimuli. Networks of developing brain cells change their morphology and function in response to external stimulation. The neural network is said to have plasticity. Plasticity involves long-term changes in synaptic efficiency. Learning and memory are two examples of plasticity in action.

We stimulated a single neuron with an embedded electrode, and monitored the response of another neuron with a glass microelectrode, as shown in Fig. 32 (Charlety *et al.* 1994). Test stimuli of 10 ms duration and 1·2 V amplitude were applied every 10 s, but no regular response was observed.

Three different types of tetanic, or high-frequency, stimuli were applied. When a tetanic stimulation of 2 V amplitude and 100 ms width was applied, again no regular response appeared. When the tetanic stimulus was applied, and the monitored neuron was kept in an excited state by depolarising potentiation of 40 mV, a regular train of pulse responses appeared, but it disappeared in a short time. Finally, a regular and persistent train of responses was obtained when

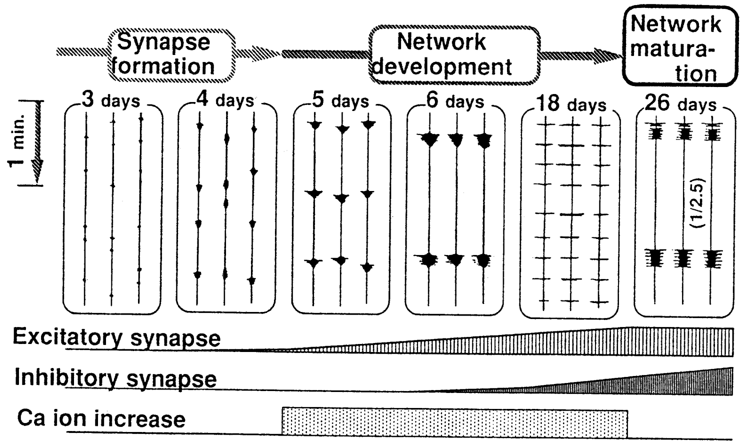

Fig. 31. Development of a neural cell network.

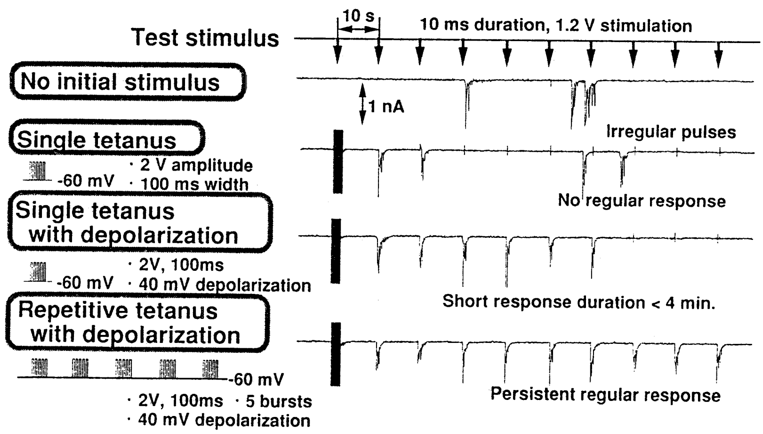

Fig. 32. Neural cell network—long term potentiation by tetanic stimuli.

◇Semiconductor physics

Surface structure transition of GaAs, InAs and Si

H. Yamaguchi, K. Shiraishi, M. Kasu, *M. Ekenstedt, *B. A. Joyce, Y. Horikoshi, H. Hibino, T. Fukuda, K. Prabhakaran, *R. Hull, T. Ogino

Electron transport in low-dimensional structure

Y. Hirayama, T. Fujisawa, *T. Bever, *A. D. Wieck, *D. G. Austing, *G. E. Bauer, *T. Wang, S. Tarucha, J. Nitta, *J. B. Hansen, *N. van der Post, H. Takayanagi

◇Quantum optics

Microcavity quantum-wire semiconductor laser

*F. Machinaga, *H. Heitmann, *G. Bjork, *R. J. Horowicz, *A. Karlson, *X. Xiong, S. Machida, T. Mukai, Y. Yamamoto, A. Chavez-Pirson, H. Saito, H. Ando, H. Kanbe, N. Kobayashi

Quantum nondemolition (QND) measurement of fiber soliton

S. Friberg, *H. A. Haus, *P. P. Drummond, *R. J. Hawkins, *W. Jiang, *W. Delong, S. Machida, T. Mukai, Y. Yamamoto

◇Biological electronics

Artificial network development of cultivated neural cells

Y. Jinbo, E. Maeda, H. Kamioka, *P. Gogan, *M. Meister, *H. Robinson, *P. Charlety, A. Kawana

*Invited scientists, post docs., and trainees

Fig. 33. Recent research topics of interest at the NTT Basic Research Laboratories.

repetitive tetanic stimulation was combined with the depolarisation, as shown at the bottom of Fig. 32. This result suggests that the stimulation induces a new signal transmission pathway.

During the network development, the number of synaptic connections must increase, and the network must be transformed by improving the synaptic transmission efficiency. Since this type of stimulation is similar to the periodic burst shown in Fig. 31, these results suggest that the periodic bursts have the potential to induce network plasticity during development.

7. Conclusion

Fig. 33 again lists the topics discussed here and gives the names of the scientists involved. The number of scientists engaged in these works is, in all, about 50. Visiting scientists, whose names are shown in red and by an asterisk, comprise about 50 per cent. We enjoy the fruits of successful joint research thanks to close international collaboration. Personnel exchange boosts the productivity of our complex. At the same time, the collaborative work also provides an excellent research environment for educating younger-generation scientists. The NTT Basic Research Laboratories are committed to continuous, lively exchange of ideas to spur advances.

Acknowledgment

The author would like to thank H. Yamaguchi, K. Shiraishi, H. Hibino, Y. Hirayama, S. Tarucha, H. Takayanagi, T. Mukai, H. Ando, S. Friberg, Y. Jimbo and A. Kawana for their help in preparing the manuscript.

References

Al'tshuler, B. L., and Spivak, B. Z. (1987). *Sov. Phys. JETP* **65**, 343.
Bever, T., Hirayama, Y., and Tarucha, S. (1995). *Japan. J. Appl. Phys.* **33**, L800.
Charlety, P. J., Jimbo, Y., Maeda, E., Kamioka, H., and Kawana, A. (1994). 24th Annual Meeting of the Society for Neuroscience, Miami.
Chavez-Pirson, A., Ando, H., Saito, H., and Kanbe, H. (1993). *Appl. Phys. Lett.* **62**, 3082.
Chavez-Pirson, A., Ando, H., Saito, H., and Kanbe, H. (1994). *Appl. Phys. Lett.* **64**, 1759.
Drummond, P. D., Shelby, R. M., Friberg, S. R., and Yamamoto, Y. (1993). *Nature* **365**, 307.
Friberg, S. R., Machida, S., Imoto, N., Watanabe, K., and Mukai, T. (1994). 19th Int. Quantum Electronics Conf., Anaheim, Ca., U.S.A., post-deadline paper.
Fujisawa, T., Hirayama, Y., and Tarucha, S. (1994). *Appl. Phys. Lett.* **64**, 2250.
Fukui, T., Saito, H., and Tokura, Y. (1988). *Japan. J. Appl. Phys.* **27**, L1320.
Fukuyama, H., and Maekawa, S. (1986). *J. Phys. Soc. Japan* **55**, 1814.
Hibino, H., and Ogino, T. (1994). *Phys. Rev. Lett.* **72**, 657.
Hibino, H., Fukuda, T., Suzuki, M., Homma, Y., Sato, T., and Iwatsuki, M. (1993). *Phys. Rev.* B **47**, 13027.
Hirayama, Y., and Tarucha, S. (1993). *Appl. Phys. Lett.* **63**, 2366.
Horikoshi, Y., Kawashima, M., and Yamaguchi, H. (1986). *Japan. J. Appl. Phys.* **25**, L868.
Horowitz, R., Heitman, H., Kadota, Y., and Yamamoto, Y. (1992). *Appl. Phys. Lett.* **61**, 393.
Jimbo, Y., Robinson, H. P. C., and A. Kawana, A. (1993). *IEEE Trans. Biomedical Eng.* **40**, 804.
Jimbo, Y., Robinson, H. P. C., Maeda, E., Kuroda, Y., and Kawana, A. (1994). 24th Annual Meeting of the Society for Neuroscience, Miami.
Machinaga, F. M., Karlsson, A., Machida, S., Yamamoto, Y., Suzuki, T., Kadota, Y., and Ikeda, M. (1993). *Appl. Phys. Lett.* **62**, 443.
Pashley, M. D., and Haberern, K. W. (1991). *Phys. Rev. Lett.* **67**, 2697.

Pashley, M. D., Haberern, K. W., Feenstra, R. M., and Kirchner, P. D. (1993). *Phys. Rev.* B **48**, 4612.
Saito, H., Uwai, K., and Kobayashi, N. (1993*a*). *Japan. J. Appl. Phys.* **32**, 4440.
Saito, H., Uwai, K., and Tokura, Y. (1993*b*). *Appl. Phys. Lett.* **63**, 72.
Shiraishi, K., Ito, T., and Ohno, T. (1994). *Solid-State Electron.* **37**, 601.
Suzuki, M., Hibino, H., Homma, Y., Fukuda, T., Sato, T., Iwatsuki, M., Miki, K., and Tokumoto, H. (1993*a*). *Japan. J. Appl. Phys.* **32**, 3247.
Suzuki, M., Homma, Y., Hibino, H., Fukuda, T., Sato, T., Iwatsuki, M., Miki, K., and Tokumoto, H. (1993*b*). *J. Vac. Sci. Tech.* A **11**, 1640.
Takayanagi, H., Hansen, J. B., and Nitta, J. (1995*a*). *Phys. Rev. Lett.* (to be published).
Takayanagi, H., Hansen, J. B., and Nitta, J. (1995*b*). *Phys. Rev. Lett.* (to be published).
Yamaguchi, H., and Horikoshi, Y. (1992). *Phys. Rev.* B **45**, 1511.
Yamaguchi, H., and Horikoshi, Y. (1993*a*). *Phys. Rev. Lett.* **70**, 1299.
Yamaguchi, H., and Horikoshi, Y. (1993*b*). *J. Crystal Growth* **127**, 976.
Yamaguchi, H., and Horikoshi, Y. (1995*a*). *Japan J. Appl. Phys.* **33**, L1423.
Yamaguchi, H., and Horikoshi, Y. (1995*b*). (to be submitted).

Manuscript received 30 June, accepted 28 October 1994